Research Square

Preprints are preliminary reports that have not undergone peer review.
They should not be considered conclusive, used to inform clinical practice,
or referenced by the media as validated information.

Over-injection of time-correlated tropospheric constraints induces PPP height shifts: a Gauss–Markov remedy

Jing WU
Hong Kong Polytechnic University
Zhizhao Liu
george.liu@polyu.edu.hk

Hong Kong Polytechnic University https://orcid.org/0000-0001-6822-9248

Research Article

Keywords: Precise point positioning, External tropospheric constraint, Zenith wet delay, Gauss–Markov process, Time-correlated errors, Station height shift

Posted Date: November 6th, 2026

DOI: https://doi.org/10.21203/rs.3.rs-11637033/v1

License: This work is licensed under a Creative Commons Attribution 4.0 International License.
Read Full License

Additional Declarations: The authors declare no competing interests.

Over-injection of time-correlated tropospheric constraints induces PPP height shifts: a Gauss–Markov remedy

Jing Wu[1] · Zhizhao Liu[1,*]

[1] Department of Land Surveying and Geospatial Science, The Hong Kong Polytechnic University, Hung Hom, Kowloon, Hong Kong, China

* Corresponding author: Zhizhao Liu, e-mail: george.liu@polyu.edu.hk

ORCID: Zhizhao Liu 0000-0001-6822-9248

Abstract

External zenith total delay (ZTD) constraints improve precise point positioning (PPP) but are commonly treated as temporally independent epoch-wise pseudo-observations. Their errors exhibit substantial temporal correlation. Neglecting this correlation can over-inject constraint information and distort PPP height through its strong coupling with ZTD. This study uses ZTD derived from the fifth-generation European Centre for Medium-Range Weather Forecasts reanalysis (ERA5) to quantify the resulting height effects. Treating the ZTD constraint errors as white noise overestimates their effective information content by a factor of about 65 relative to that implied by the residual autocorrelation, while the magnitude of the ZTD-to-height leakage coefficient reaches 1.74 in static mode and 1.93 in kinematic mode. To handle this temporal correlation, the constraint residuals are modeled as a combination of a diurnal cycle, a daily constant offset, and a time-correlated component described by a first-order Gauss–Markov process, with the constant offset and the Gauss–Markov process introduced as additional filter states. Results show that the proposed approach not only retains the convergence gain over the unconstrained solution but also substantially mitigates the constraint-induced height shifts. The magnitude of the ZTD-to-height leakage coefficient decreases to 0.08 in static mode and 0.11 in kinematic mode, the median absolute height difference from the

unconstrained solution in static mode decreases from 9.4 to 0.4 mm, and the discrepancy between the filter-reported formal height uncertainty and the empirical height error is substantially reduced.

Keywords

Precise point positioning · External tropospheric constraint · Zenith wet delay · Gauss–Markov process · Time-correlated errors · Station height shift

Acknowledgments

The authors thank the International GNSS Service (IGS) for providing the GNSS observations and tropospheric products, and the European Centre for Medium-Range Weather Forecasts (ECMWF) for the ERA5 reanalysis products.

1 Introduction

Precise point positioning (PPP) can achieve centimeter-level accuracy with a single receiver, but it usually requires a long convergence time. The slow convergence stems partly from the near collinearity of the zenith wet delay (ZWD) and station height in the observation model, which makes the two parameters difficult to separate until sufficient geometric diversity accumulates over time (Santerre 1991). To reduce the coupling between the ZWD and station height and thereby shorten the convergence time, a common implementation is to introduce the external zenith total delay (ZTD) as an epoch-wise pseudo-observation. Tropospheric delays from regional GNSS networks, numerical weather prediction (NWP) models and reanalysis products have all been used for this purpose (Shi et al. 2014; Lu et al. 2016; Yao et al. 2017; Wilgan et al. 2017; Aggrey and Bisnath 2019; Huang et al. 2023; Gao et al. 2024; Ma et al. 2025; Dehvari et al. 2025; Deng et al. 2026).

A common implementation is to introduce the external zenith total delay (ZTD) as an epoch-

wise pseudo-observation, whose uncertainty is represented by independent white noise with an empirically chosen variance (Li et al. 2015; Yao et al. 2017). However, the errors of external tropospheric products are not temporally independent. External ZTD errors generally contain pronounced low-frequency components and exhibit substantial serial correlation, reflecting the slowly varying nature of atmospheric water vapor as well as persistent modeling and representativeness errors (Tralli and Lichten 1990; Bock and Parracho 2019). Ibrahim and El-Rabbany (2011) found that the residuals of a NWP-derived ZTD product relative to IGS estimates remain correlated over intervals of hours and modeled their covariance with first-order Gauss–Markov and exponential-cosine functions, while Gallon et al. (2021) derived bounded Gauss–Markov models of the residual tropospheric delay for integrity monitoring.

In conventional real-time PPP, the Kalman filter is commonly employed, with the measurement errors assumed to be temporally uncorrelated. However, the temporal correlation of errors in external ZTD pseudo-observations is inconsistent with this assumption (Khodabandeh et al. 2022). The strong correlation between successive constraint errors means that each epoch adds little independent information, whereas the filter, which treats the errors as uncorrelated, accumulates weight in proportion to the number of epochs, so that the constraint information is over-injected. Since the ZWD and station height are nearly collinear, this excess information is not confined to the ZWD estimate but also propagates into the height solution. Yao et al. (2017) found that applying an external product as a fixed correction displaces the estimated height from its reference value. This corresponds to the limiting case in which the constraint receives infinite weight. They attributed the displacement primarily to the limited accuracy of the external product. As a remedy, they proposed an empirical stochastic model in which the constraint variance is set to twice the square of nine times the root-mean-square error of the product. Although effective, this factor was determined from 30-s data and was not related to the sampling interval or to the temporal correlation of the product error, both of which govern

how much independent information a constraint series carries. These findings motivate a quantitative investigation of how neglecting temporal correlation in external ZTD constraint errors affects the information accumulated across epochs and how this information propagates into PPP height estimates.

Using ERA5-derived ZTD as external pseudo-observations, this study first characterizes the temporal structure of the constraint errors and its variation across climate bands. The information over-injection induced by the epoch-wise independence assumption is then quantified, and how this excess propagates into the coordinate solution is investigated, with particular emphasis on constraint-induced arc-level height shifts and the consistency between the filter-reported formal uncertainty and empirical error. Finally, we represent the correlated constraint error within the PPP filter by a constant offset and a first-order Gauss–Markov process and evaluate the new scheme against the empirical remedy described above.

2 Methodology

2.1 PPP with epoch-wise external ZTD pseudo-observations

The PPP estimator is formulated as a discrete-time Kalman filter with the following state transition and linearized observation models (Kalman 1960):

$$\mathbf{x}_k = \mathbf{\Phi}_{k,k-1}\mathbf{x}_{k-1} + \mathbf{w}_k \quad (1)$$

$$\mathbf{y}_k = \mathbf{H}_k\mathbf{x}_k + \mathbf{v}_k \quad (2)$$

Here, $\mathbf{x}_k$ is the state vector, $\mathbf{\Phi}_{k,k-1}$ denotes the state transition matrix, and $\mathbf{y}_k$ represents the linearized observation vector with design matrix $\mathbf{H}_k$. The process noise $\mathbf{w}_k$ and measurement noise $\mathbf{v}_k$ are assumed to be zero-mean, temporally uncorrelated, mutually uncorrelated and uncorrelated with the initial state, with known covariance matrices $\mathbf{Q}_k$ and $\mathbf{R}_k$, respectively.

Under these assumptions, the predicted error covariance is $\mathbf{P}_{k|k-1} =$

$\mathbf{\Phi}_{k,k-1}\mathbf{P}_{k-1|k-1}\mathbf{\Phi}_{k,k-1}^{\mathrm{T}} + \mathbf{Q}_k$, and the measurement update takes the information form (Simon 2006)

$$\mathbf{P}_{k|k}^{-1} = \mathbf{P}_{k|k-1}^{-1} + \mathbf{H}_k^{\mathrm{T}}\mathbf{R}_k^{-1}\mathbf{H}_k \tag{3}$$

Each measurement update adds the nominal information contribution $\mathbf{H}_k^{\mathrm{T}}\mathbf{R}_k^{-1}\mathbf{H}_k$ to the filter-reported inverse covariance. When temporally correlated ZTD constraints are treated as independent white noise, partly redundant constraint information is counted repeatedly across epochs, causing the filter-reported formal covariance to underestimate the true error variance of the resulting suboptimal estimator.

The ionosphere-free pseudorange and carrier-phase observation equations(Kouba and Héroux 2001) for satellite s at epoch k are given by

$$P_k^s = \rho_k^s + cdt_{r,k} + T_k^s + e_{P,k}^s \tag{4}$$

$$L_k^s = \rho_k^s + cdt_{r,k} + T_k^s + B_k^s + e_{L,k}^s \tag{5}$$

where ρ_k^s is the geometric range, $cdt_{r,k}$ the receiver clock offset, T_k^s the slant tropospheric delay and B_k^s the ionosphere-free phase ambiguity. The slant tropospheric delay is decomposed as

$$T_k^s = m_h(E_k^s)T_{h,k}^0 + m_w(E_k^s)\left(Z_k - T_{h,k}^0\right) \tag{6}$$

where $T_{h,k}^0$ is the a priori hydrostatic delay from the Saastamoinen model (Saastamoinen 1972), m_h and m_w the hydrostatic and wet Niell mapping functions (Niell 1996) at elevation E_k^s, and Z_k the ZTD state estimated by the filter. The difference $Z_k - T_{h,k}^0$ represents the estimated ZWD and is mapped to the slant direction using m_w. After applying the a priori corrections and

linearizing Eqs. (4) and (5) about the predicted state, with the coordinate increments $\mathbf{\Delta r}_k$ resolved in the local east–north–up frame, the observation model of Eq. (2) can be written as

$$\begin{bmatrix} \Delta P_k^1 \\ \Delta L_k^1 \\ \vdots \\ \Delta P_k^n \\ \Delta L_k^n \end{bmatrix} = [-\mathbf{U}_k \quad \mathbf{1} \quad \mathbf{m}_{w,k} \quad \mathbf{D}_k] \begin{bmatrix} \mathbf{\Delta r}_k \\ cdt_{r,k} \\ Z_k \\ \mathbf{B}_k \end{bmatrix} + \mathbf{v}_k \tag{7}$$

where n denotes the visible satellite number, $\mathbf{U}_k$ stacks the receiver-to-satellite unit vectors, $\mathbf{m}_{w,k}$ the wet mapping function values, and $\mathbf{D}_k$ maps each carrier-phase observation to its corresponding ambiguity. In the linearized observation model, the partial derivatives with respect to the receiver clock term $cdt_{r,k}$, station height, and ZTD are 1, $-\sin E_k^s$, and $m_w(E_k^s)$, respectively. Over the observed elevation range, the wet-mapping column has a large projection onto the subspace spanned by the clock and height columns. Consequently, an error in the ZTD state can be substantially absorbed by the receiver clock and height estimates. This near-collinearity underlies the strong ZWD–height correlation in PPP (Santerre 1991); its consequences for the constrained solution are quantified in Sect. 2.4.

ZTD-constrained PPP (Yao et al. 2017) introduces the external ZTD $T_{ext,k}$ directly as a pseudo-observation of the ZTD state,

$$T_{ext,k} = Z_k + \varepsilon_k \tag{8}$$

where ε_k is the constraint error. Equation (8) adds to Eq. (7) a row whose design vector $[\mathbf{0} \quad 0 \quad 1 \quad \mathbf{0}]$ acts on the ZTD state alone, with the variance σ_c^2 of ε_k. In the conventional white-noise constraint-error model,

$$E(\varepsilon_k \varepsilon_j) = \begin{cases} \sigma_c^2 & j = k \\ 0 & j \neq k \end{cases} \quad (9)$$

with σ_c set from the accuracy of the product. This model describes the error of the external pseudo-observation, not the temporal evolution of Z_k, which is governed separately by the random-walk process noise of the ZTD state. Whether ε_k satisfies Eq. (9) is examined in Sect. 2.2.

2.2 Temporal structure of external ZTD constraint errors

The constraint error ε_k in Eq. (8) is estimated from the difference between the external ZTD and the more precise IGS final tropospheric product,

$$\hat{\varepsilon}_k = T_{\mathrm{ext},k} - T_{\mathrm{IGS},k} \quad (10)$$

Residuals are formed at the hourly epochs of the external product using the corresponding IGS estimates. The white-noise assumption in Eq. (9) is examined using their sample autocorrelation at integer-hour lags.

To represent the temporal structure of the constraint error, ε_k is decomposed as

$$\varepsilon_k = D(t_k) + a + b_k + \eta_k \quad (11)$$

Here, $D(t)$ represents the deterministic diurnal variation and is modeled using 24-h and 12-h harmonics,

$$D(t) = d_1 \cos\left(\frac{2\pi t}{24\,\mathrm{h}} + \varphi_1\right) + d_2 \cos\left(\frac{2\pi t}{12\,\mathrm{h}} + \varphi_2\right) \quad (12)$$

with amplitudes d_1 and d_2 and phases φ_1 and φ_2. The random offset a, with prior variance σ_a^2, is constant within each daily arc but varies between arcs. It may combine station-dependent systematic effects and daily offsets, which cannot be distinguished within a single arc. The

temporally uncorrelated component η_k has variance σ_η^2 and represents variability unresolved by the hourly sampling. The correlated component b_k follows a first-order Gauss–Markov process,

$$b_k = e^{-\Delta t/\tau}\, b_{k-1} + \xi_k, \quad E(\xi_k^2) = \sigma_b^2\left(1 - e^{-2\Delta t/\tau}\right) \tag{13}$$

where τ is the e-folding correlation time, σ_b^2 is the stationary variance of b_k, and Δt is the sampling interval. The white-noise model in Eq. (9) is recovered when $D(t) = a = b_k = 0$ and $\sigma_c^2 = \sigma_\eta^2$.

For each station–month, the diurnal cycle is fitted by least squares to daily-demeaned residuals pooled over the month. For ACF estimation, the fitted cycle is removed from the original residuals, which are then centered on the monthly mean without further daily demeaning. Within-day autocorrelations are normalized by each day's mean square and averaged over the month, weighted by the number of available pairs at each lag. This yields $\hat{\rho}(\Delta)$ for $\Delta = 1, \ldots, 23$ h, which is fitted with

$$\rho(\Delta) = A\, e^{-\Delta/\tau} + C + B_1 \cos\left(\frac{2\pi\Delta}{24\ \mathrm{h}}\right) + B_2 \cos\left(\frac{2\pi\Delta}{12\ \mathrm{h}}\right) \tag{14}$$

where A and C are the coefficients of the exponential and constant terms of the normalized ACF, respectively, while B_1 and B_2 describe residual 24-h and 12-h periodic correlation, respectively. The ACF is fitted by equally weighted least squares, excluding zero lag; the harmonic terms are excluded from the PPP filter. The amplitude is constrained to $0 \le A \le 1.5$, and the Gauss–Markov standard deviation is calibrated as $\sigma_b = \sqrt{A}\, s$, with s the sample standard deviation of the monthly residual series after removing the diurnal cycle and monthly mean. The fitted correlation time and calibrated GM standard deviation are passed to the PPP filter, while the offset and GM states are estimated within the filter. The correlation-time search range

is 12 min–24 h; estimates below 15 min or above 1400 min are treated as boundary-affected and replaced by the median valid estimate for the same climate band and month.

2.3 Quantifying information over-injection through the effective sample size

For the ZTD pseudo-observation in Eq. (8), each measurement update contributes $1/\sigma_c^2$ to the information associated with the ZTD state. At the adopted 300-s injection interval, a daily arc contains $N = 288$ pseudo-observations, giving an accumulated constraint weight of N/σ_c^2 under the white-noise assumption. The hourly product is linearly interpolated to the update epochs, but its errors are temporally correlated. The effective sample size quantifies the number of independent constraints (Bayley and Hammersley 1946),

$$N_{\text{eff}} = \frac{N}{1 + 2\sum_{j=1}^{N-1}\left(1 - \frac{j}{N}\right)\rho(j\Delta t)} \tag{15}$$

where $\Delta t = 300\,s$ and ρ is the autocorrelation of the stochastic constraint error. The exponential and constant components identified in Eq. (14) are evaluated at multiples of Δt to represent correlation at the 300-s constraint update epochs under the continuous-lag stationary model.

The information over-injection factor is defined as

$$F = \frac{N}{N_{\text{eff}}} \tag{16}$$

F measures how much the white-noise assumption overstates the effective number of independent constraints and depends on error correlation, injection interval and arc length.

Let γ_{WN} denote the fraction of the ZTD information attributed to the constraint under the white-noise model. Replacing the nominal constraint weight N/σ_c^2 by its effective value $N_{\text{eff}}/\sigma_c^2$ gives

$$\gamma_{\text{eff}} = \frac{\gamma_{\text{WN}}}{\gamma_{\text{WN}} + F(1 - \gamma_{\text{WN}})} \tag{17}$$

The effective weight applies to the arithmetic mean over an arc, not the full information in a time-varying PPP filter. Its interpretation assumes a common marginal variance and a covariance model valid at the constraint injection epochs. The derivation and covariance assumptions are given in Online Resource 1 (Sect. S1.4, which also details the exact covariance propagation $R_{inj} = LR_{hour}L^T$ when 300-s constraints are obtained by linear interpolation of hourly products).

2.4 ZTD-to-height error propagation

To quantify how excess ZTD constraint information affects station height, consider a reduced linear model with parameter vector $\mathbf{x}$, in which Z and U denote the ZTD and station-height components, respectively. Let $\mathbf{N}_0$ be the normal matrix of the unconstrained ZTD solution and $\mathbf{Q}_0 = {\mathbf{N}_0}^{-1}$ its formal covariance matrix. The vectors $\mathbf{e}_Z$ and $\mathbf{e}_U$ select the corresponding components.

An external ZTD constraint with scalar information q contributes $q\mathbf{e}_Z{\mathbf{e}_Z}^T$ to the normal matrix. For arc-mean error δ, the right-hand-side perturbation is $q\mathbf{e}_Z\delta$. The resulting constraint-induced parameter increment, relative to the unconstrained solution, is

$$\begin{aligned} \mathbf{\Delta x}_\delta &= (\mathbf{N}_0 + q\mathbf{e}_Z{\mathbf{e}_Z}^T)^{-1} q\mathbf{e}_Z\delta \\ &= \frac{q\mathbf{Q}_0\mathbf{e}_Z}{1 + q{\mathbf{e}_Z}^T\mathbf{Q}_0\mathbf{e}_Z}\delta \end{aligned} \tag{18}$$

where the second equality follows from the Sherman–Morrison identity. Projecting this constraint-induced parameter increment onto the height component gives

$$\begin{gathered} \Delta U_\delta = \kappa\gamma\delta, \\ \kappa = \frac{{\mathbf{e}_U}^T\mathbf{Q}_0\mathbf{e}_Z}{{\mathbf{e}_Z}^T\mathbf{Q}_0\mathbf{e}_Z}, \quad \gamma = \frac{q{\mathbf{e}_Z}^T\mathbf{Q}_0\mathbf{e}_Z}{1 + q{\mathbf{e}_Z}^T\mathbf{Q}_0\mathbf{e}_Z}. \end{gathered} \tag{19}$$

Here, κ is the ZTD–height geometric coupling coefficient in the unconstrained adjustment, accounting for the other estimated parameters. The dimensionless factor γ is the fraction of the total scalar ZTD information supplied by the external constraint in this reduced model. For fixed κ and δ, increasing the assigned constraint information increases γ and amplifies the constraint-induced height increment; neglecting temporal correlation can therefore amplify this increment through excessive constraint weighting. Note that Eq. (19) describes the conditional height shift within a given daily arc for a specific realization of the arc-mean error δ. Across an ensemble of arcs where δ has zero mean, neglecting temporal correlation does not introduce an unconditional bias in expectation, but inflates the true error variance of the height estimator in proportion to $(\kappa\gamma)^2$.

Because the full PPP filter involves time-varying ZTD dynamics and temporally structured constraint errors, the reduced-model relation is used only as a scalar approximation of the constraint-induced height increment,

$$\Delta U \approx \kappa\gamma\delta, \tag{20}$$

where ΔU is the Up-coordinate difference between the constrained and corresponding unconstrained PPP solutions. The coefficient κ is obtained from the linearized PPP normal equations, while γ is evaluated independently in the ZTD domain for each processing scheme; neither is estimated from the empirical ΔU–δ regression. For each station-day, ΔU is paired with the arc-mean constraint error δ, and the least-squares slope is compared with $\kappa\gamma$ for static and kinematic processing under each constraint-weighting scheme. This interpretation requires negligible covariance between the scalar-approximation error and δ and, when gains vary across station-days, consistent regression weights and intercept treatment for theoretical predictions and empirical increments. The derivation and applicability conditions are given in Online Resource 1.

2.5 Modeling ZTD constraint errors with constant and Gauss–Markov states

The PPP state vector is augmented with an arc-constant offset a and a first-order Gauss–Markov component b_k to represent persistent and time-varying constraint errors, respectively. Only the external constraint-error model is augmented; the ZTD state retains its original random-walk dynamics.

Let $\mathbf{x}_k$ denote the original PPP state vector. Assuming the Gauss–Markov driving noise is uncorrelated with the original PPP process noise, the augmented model is

$$\tilde{\mathbf{x}}_k = [\mathbf{x}_k{}^{\mathrm{T}} \quad b_k \quad a]^{\mathrm{T}}, \quad \tilde{\mathbf{x}}_k = \tilde{\mathbf{\Phi}}_{k,k-1}\tilde{\mathbf{x}}_{k-1} + \tilde{\mathbf{w}}_k, \tag{21}$$

$$\begin{aligned} \tilde{\mathbf{\Phi}}_{k,k-1} &= \begin{bmatrix} \mathbf{\Phi}_{k,k-1} & \mathbf{0} & \mathbf{0} \\ \mathbf{0}^{\mathrm{T}} & \varphi & 0 \\ \mathbf{0}^{\mathrm{T}} & 0 & 1 \end{bmatrix}, \\ \tilde{\mathbf{Q}}_k &= \begin{bmatrix} \mathbf{Q}_k & \mathbf{0} & \mathbf{0} \\ \mathbf{0}^{\mathrm{T}} & \sigma_b^2(1-\varphi^2) & 0 \\ \mathbf{0}^{\mathrm{T}} & 0 & 0 \end{bmatrix}, \end{aligned} \tag{22}$$

where $\varphi = \exp(-\Delta t/\tau)$ is the discrete-time Gauss–Markov transition coefficient, and Δt denotes the propagation interval. The parameters τ and σ_b denote the correlation time and stationary standard deviation of the Gauss–Markov component, respectively. The arc-constant offset a has unit transition and zero process noise within each arc. Its initial uncertainty is specified by the prior variance σ_a^2.

The augmented error states enter only the external ZTD pseudo-observation; the GNSS observation model is unchanged. The combined system is

$$\begin{bmatrix} \mathbf{y}_k \\ T_{\mathrm{ext},k} \end{bmatrix} = \begin{bmatrix} \mathbf{H}_k & \mathbf{0} & \mathbf{0} \\ \mathbf{e}_Z{}^{\mathrm{T}} & 1 & 1 \end{bmatrix} \tilde{\mathbf{x}}_k + \begin{bmatrix} \mathbf{v}_k \\ v_{\mathrm{c},k} \end{bmatrix}, \tag{23}$$

where $\mathbf{e}_Z$ selects the ZTD component of the original PPP state, and $v_{\mathrm{c},k}$ denotes the residual constraint error after accounting for the augmented components. $v_{\mathrm{c},k}$ is assumed to be white

noise. For stochastic parameter identification, the diurnal component $D(t_k)$ in Eq. (11) is subtracted from the original residual series so that deterministic diurnal periodicity does not bias the ACF-based estimation of τ and σ_b. All constrained schemes in Table 2 use the same diurnally corrected external ZTD series. In real-time applications where in-sample monthly harmonics are unavailable, smooth diurnal variations can either be approximated using prior-month harmonics or absorbed online by the slow Gauss–Markov state b_k and constant state a. Although Z_k, b_k, and a enter Eq. (23) as a sum, they remain jointly observable because Z_k is simultaneously constrained by multi-satellite GNSS observations through the elevation-dependent wet mapping function $m_w(E_k^s)$ in Eq. (7), whereas b_k and a appear only in the pseudo-observation equation. Their distinct prior variances and process dynamics govern the information allocation across time: during initial convergence when satellite geometry is weak, the bounded prior variances of a and b_k allow the external constraint to pull Z_k and accelerate height convergence; as satellite geometry strengthens and GNSS observations accumulate information on Z_k, persistent offsets and slow within-day correlated errors in $T_{\mathrm{ext,k}}$ are absorbed into a and b_k rather than displacing Z_k and station height. Within the recursive Kalman filter, augmenting the state vector with the zero-mean random states a and bk accounts for the temporal error covariance of the external constraints, reducing the true estimation error variance relative to the misspecified white-noise filter.

The augmented filter uses station–month estimates of τ and σ_b derived from the external–IGS ZTD residuals. Initialization and noise settings are summarized in Table 2. The Gauss–Markov state is propagated using the elapsed time between consecutive PPP epochs, while external ZTD constraints are applied at nominal 300-s intervals.

2.6 Data, processing schemes and evaluation metrics

In the study, GNSS observations from January and July 2025 for 30 stations spanning five climatic regimes: tropical, arid, temperate, boreal, and polar were used to demonstrate the

advantages of our proposed method in the static and kinematic PPP processing. In the PPP solutions, ERA5-derived ZTD estimates provided external constraints. IGS final tropospheric and SINEX coordinates products were used as the references to assess the errors of external ZTD and PPP solution.

Static and kinematic PPP solutions were computed for independent station-day arcs using the common configuration summarized in Table 1.

Table 1 Basic PPP configuration used in the study

Item	**Description**
Software	Modified MADOCALIB 2.1
Observations	Dual-frequency ionosphere-free observations from GPS, GLONASS, Galileo, and QZSS
Sampling	30 s
Orbit and Clock products	WUM0MGXFIN precise orbit and clock products
Elevation cutoff	10°
Processing	Static and kinematic; independent station-day arcs
Ambiguities	Float; constant between cycle slips
Receiver clock	White noise
ZTD	Random walk (6 mm/ √ h)
Coordinates	Constant in static mode; white noise in kinematic mode
External ZTD updates	300 s (nominal)

Four schemes for ZTD estimation in the PPP processing are utilized and compared: unconstrained, white-noise constraint, the variance-inflation constraint, and our proposed GM+constant constraint scheme (Table 2). The comparison tested whether the new GM+constant constraint method could mitigate the constraint-induced height errors associated with repeated white-noise constraints while retaining early-stage positioning gains. The

advantages of our new model over the empirical variance inflation constraint proposed by Yao et al. (2017) will then be highlighted. In the white-noise scheme, each constraint update was weighted using the composite marginal variance $\sigma_c^2 = \sigma_b^2 + \sigma_{a,0}^2 + \sigma_\eta^2$ (with station–month σ_b, nominal $\sigma_{a,0}$ = 5 mm, and σ_η = 1 mm), yielding a median σ_c of 9.6 mm (range 5.4–17.0 mm across the 60 station–month combinations (30 stations × 2 months)); the variance-inflation scheme multiplied this baseline variance σ_c^2 by F ∈ {4, 16, 65, 162, 1000}.

Table 2 External ZTD constraint settings in PPP processing schemes

Scheme	Constraint weighting	Parameters	Represents
Unconstrained	None	–	Reference solution
White noise	Epoch-wise, σ_c^2 (constant, independent)	σ_c = 9.6 mm (median; 5.4–17.0 mm)	Common practice
Variance inflation	Epoch-wise, F·σ_c^2	F = 4, 16, 65, 162, 1000	Yao et al. 2017
GM + constant	Epoch-wise with augmented states a, b_k	τ, σ_b (station-month or network), σ_a = 8 mm, σ_η = 1 mm	This study

Note. For GM + constant, a and b_k are initialized to 10^{-6} m with prior variances σ_a^2 and σ_b^2, respectively. All initial cross-covariances involving these states are zero. σ_η denotes the residual constraint-noise standard deviation. Network parameters are medians across the fitted station–months (Sect. 3.5).

For each processing scheme, the empirical height error used to evaluate positioning accuracy was defined as the PPP-estimated Up coordinate minus the corresponding IGS daily SINEX reference coordinate. In contrast, the constraint-induced height increment ΔU was defined as the Up coordinate of the constrained PPP solution minus that of the corresponding unconstrained PPP solution. The dependence of ΔU on the arc-mean external ZTD constraint error (the diurnally corrected ERA5 ZTD minus the corresponding IGS final ZTD, averaged over each station-day arc) was assessed using the regression slope and R^2 in Sect. 2.4, and the

magnitude of the height response was summarized by the median absolute height increment. Positioning accuracy was evaluated using the RMS of the IGS-referenced height errors over specified time windows; the RMS reduction was calculated as the unconstrained PPP RMS minus the RMS of each constrained scheme. Uncertainty consistency was assessed by comparing formal height standard deviations with IGS-referenced empirical height errors (Fig. 10). Static and kinematic solutions were evaluated separately.

3 Results

We first characterize the temporal structure of ERA5 ZTD errors and summarize the identified Gauss–Markov parameters. We then evaluate PPP convergence and coordinate errors, compare the height response under different constraint schemes, including white-noise weighting and variance inflation, and examine the consistency between formal height uncertainty and empirical errors. Finally, we assess parameter sensitivity and the use of network-wide fixed parameters.

3.1 Temporal characteristics of external ZTD constraint errors

Atmospheric water-vapor variability contributes to both diurnal and day-to-day variations in ZTD at each station. To characterize the temporal structure of the external-constraint errors, the ERA5–IGS ZTD residuals were decomposed into three components: the diurnal cycle, a daily constant offset, and a time-correlated component, as formulated in Eq. (11). Station HOB2 is selected as an example for illustration. Figure 1 shows the decomposition of the ZTD constraint error at station HOB2 in January 2025. The hourly residuals depicted in Fig. 1a deviated substantially from the fitted diurnal cycle. After removal of the diurnal cycle, the daily constant offset varied across daily arcs (Fig. 1b). Removing the daily means eliminated the daily baseline shifts but left appreciable within-day fluctuations associated with the time-correlated component, as shown in Fig. 1c. These results indicate that the diurnal cycle explains only part of the observed variability. The daily constant offset and time-correlated component account

for the remaining day-to-day and within-day structure, respectively.

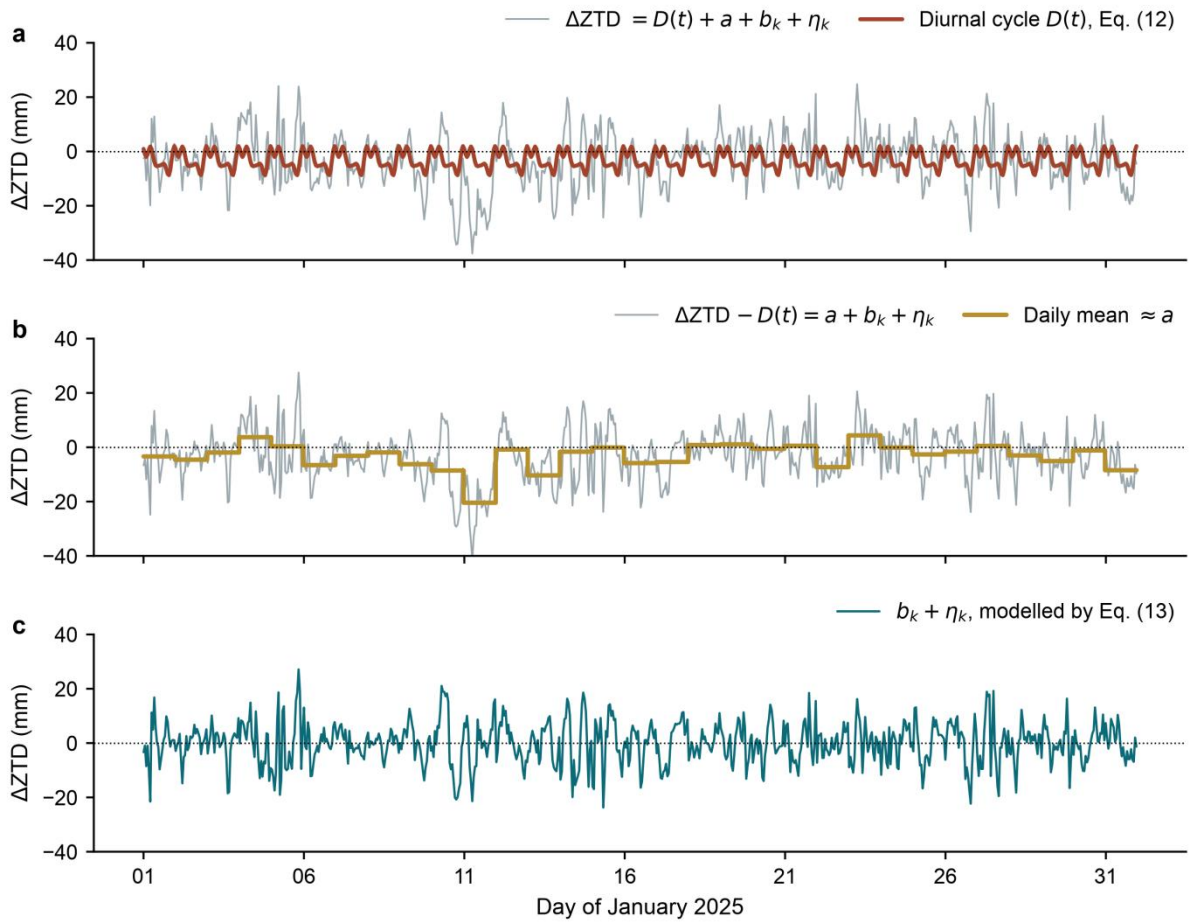


Fig. 1 Decomposition of ERA5–IGS ZTD differences at HOB2 in January 2025: a hourly differences (gray) and the fitted diurnal cycle shifted by the monthly mean for display (red); b residuals after diurnal correction (gray) and their daily means (gold); c residuals after removing both components, containing the correlated and white-noise contributions

We next analyze the residual autocorrelation to quantify temporal dependence and identify the parameters used in the constraint-error model. Figure 2 gives the ACF of ERA5–IGS ZTD residuals after removal of the fitted diurnal cycle and centering on the monthly mean at five representative stations: GUAM (tropical), AREQ (arid), HOB2 (temperate), YELL (boreal), and MAW1 (polar). The ACFs are positive at non-zero lags, in contrast to the white-noise reference, for which autocorrelation is zero at all non-zero lags. This indicates that the external ZTD constraint errors are temporally correlated and should not be modeled as epoch-wise

independent white noise. Across the five representative station–month cases, the ACFs exhibit an approximately exponential decay that is well described by a first-order Gauss–Markov (FOGM) model, with fitted correlation times (τ) ranging from 136 to 240 min, which correspond to persistence on an hourly timescale.

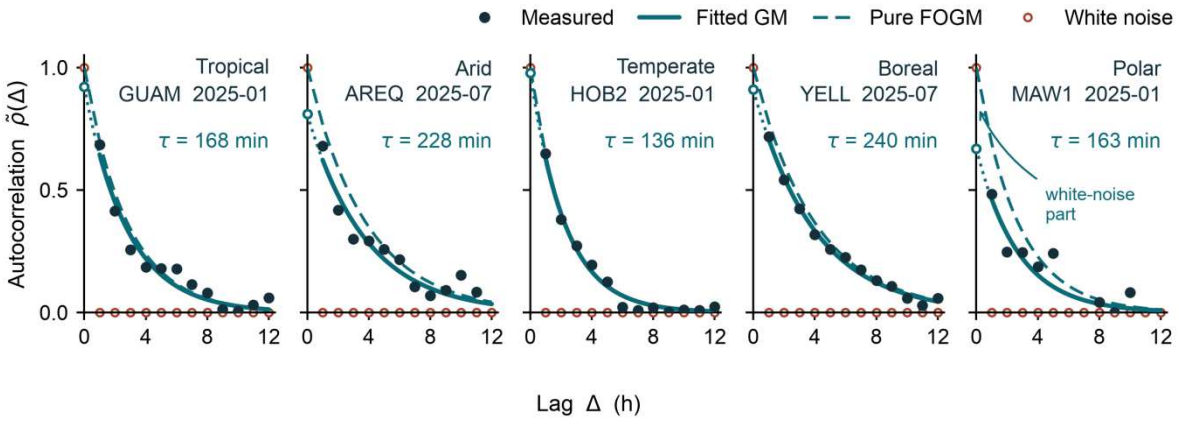


Fig. 2 Residual autocorrelation at five representative stations after diurnal correction and monthly centering, without daily demeaning. Filled circles show measured values at hourly lags; solid and dashed curves denote the fitted GM and pure FOGM curves, respectively. Open circles indicate the white-noise reference. The fitted correlation time τ is shown in each panel

To examine how the identified parameters vary across climate bands and months, the station–month estimates of τ and σ_b for January and July 2025 are summarized in Fig. 3. Both parameters exhibit appreciable within-band scatter, and the band medians vary between months. The median τ is highest in the boreal band in January, whereas the polar band has the highest median in July. For σ_b, the highest band median occurs in the tropical band in January, while the tropical and boreal bands have the highest medians in July. The polar band has among the lowest σ_b medians in both months. Overall, the ordering of band medians changes between January and July, while the spread of station-month estimates within bands indicates substantial site-level variability. The station–month estimates were obtained offline from the same months analyzed here and used in the GM + constant PPP solutions in Sects. 3.2–3.4. The present experiments therefore assess the model retrospectively; the use of parameters calibrated on

earlier data for real-time deployment remains to be validated.

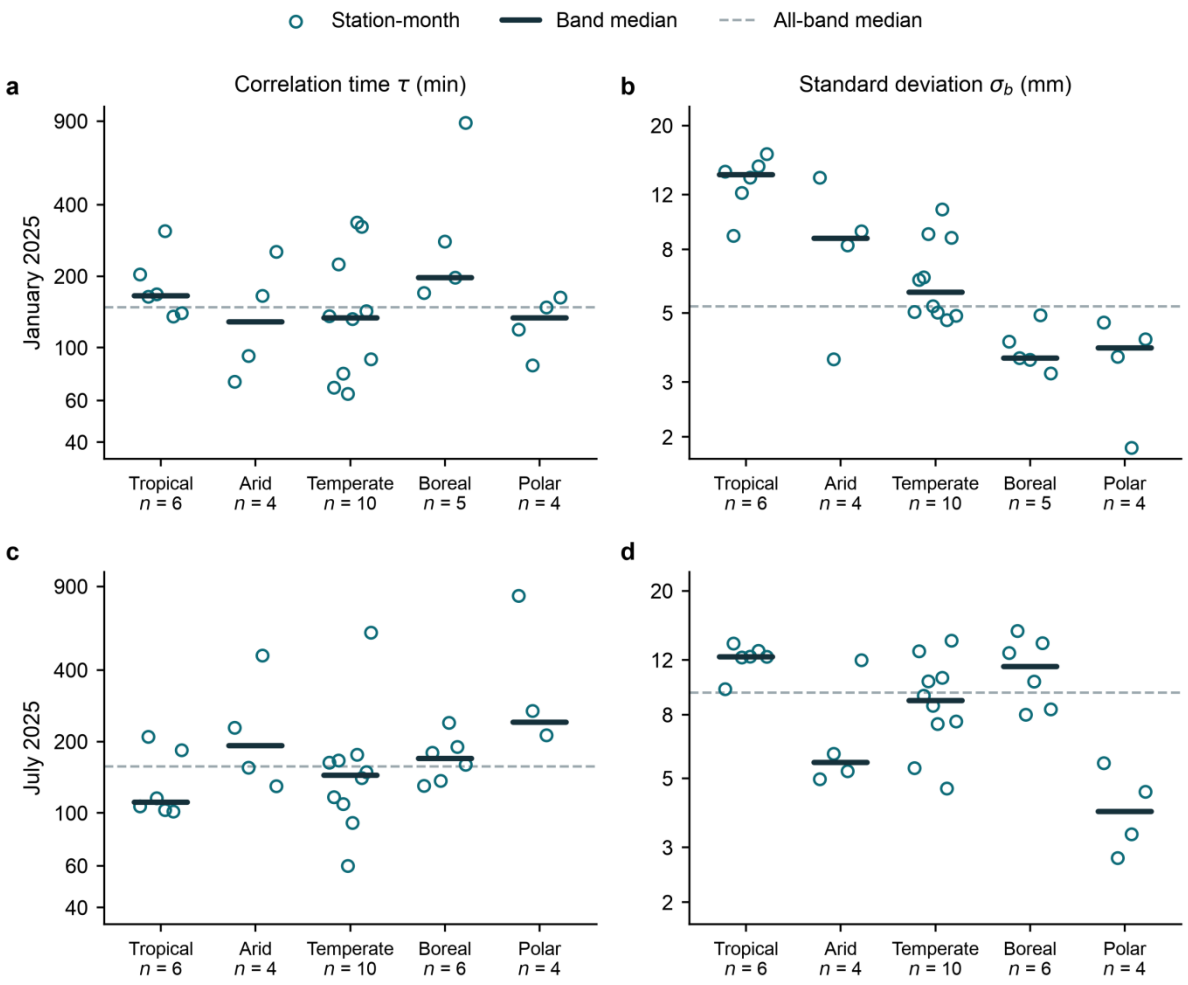


Fig. 3 Identified Gauss–Markov parameters by climate band in January 2025 **(a, b)** and July 2025 **(c, d)**. The plotted parameters are the correlation time τ (**a, c**) and the standard deviation σ_b (**b, d**). Circles denote individual station-month estimates, horizontal bars indicate climate-band medians, and dashed lines indicate the median across all bands. *n* denotes the number of station-months in each band. Both vertical axes are logarithmic

3.2 PPP convergence and coordinate errors

This section systematically demonstrates the effectiveness of our proposed ZTD constraint strategy (GM+constant constraint) in static and kinematic PPP solutions. In particular, its advantages over the conventional white-noise-constrained method are highlighted. Figure 4

shows the east, north, and up coordinate errors for the static PPP solutions with the unconstrained, white-noise, and GM + constant constraint methods at stations GUAM (tropical), ALIC (arid), NNOR (temperate), WES2 (boreal), and DAV1 (polar) on 16 January and 19 July 2025. The corresponding kinematic PPP results are illustrated in Fig. 5. Moreover, Figures 6 and 7 give the detailed convergence phase for static and kinematic PPP solutions respectively.

During the convergence phase, both constrained schemes generally attenuate Up-component transients more rapidly than the unconstrained scheme, while their effects on East and North remain modest. This directional pattern is consistent with the ZTD constraint coupling primarily to station height. However, the white-noise-constrained solutions exhibit persistent offsets in many cases, whereas the GM + constant solutions generally approach the unconstrained estimates at later epochs. Across the full two-month network (1,841–1,849 station-days), the post-convergence (2–24 h) median horizontal positioning RMS relative to the IGS daily SINEX coordinates is 10.49 mm (unconstrained), 10.50 mm (white noise), and 10.50 mm (GM + constant) in static PPP, and 22.84, 22.88, and 22.75 mm in kinematic PPP, confirming that external ZTD constraints negligibly affect horizontal accuracy. In contrast, the median post-convergence Up RMS is degraded from 10.77 mm (unconstrained) to 17.14 mm by white-noise constraints in static PPP (33.10 to 37.83 mm in kinematic PPP) and restored to 10.74 mm (32.02 mm in kinematic PPP) by the GM + constant scheme. Overall, these results clearly suggest that the GM + constant scheme retains the early convergence benefit of the external constraint while yielding Up-coordinate errors closer to zero relative to the unconstrained PPP solution at later epochs.

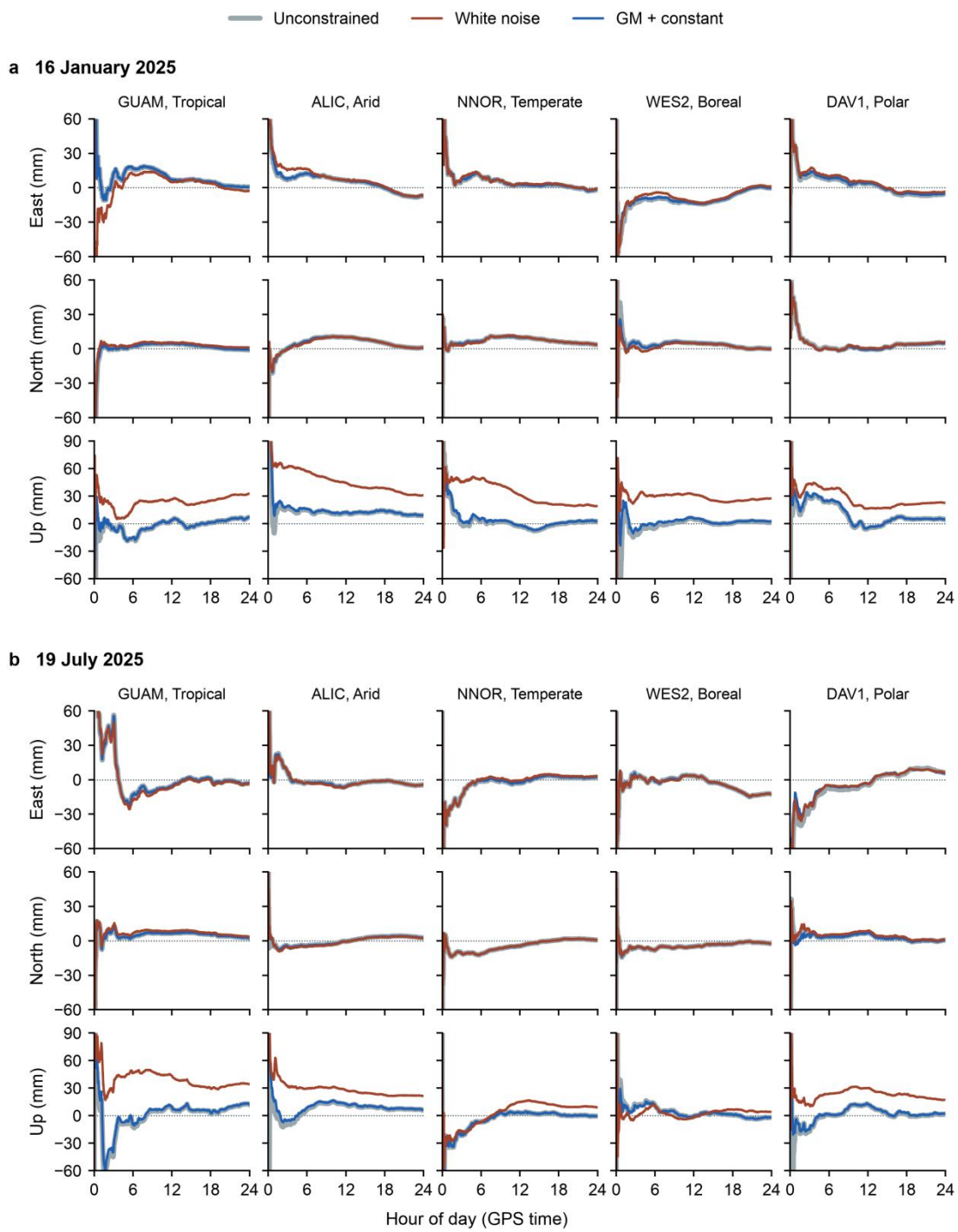


Fig. 4 East, north, and up coordinate errors for the static PPP solutions at stations GUAM (tropical), ALIC (arid), NNOR (temperate), WES2 (boreal), and DAV1 (polar) on (a) 16 January 2025 and (b) 19 July 2025. Gray, red and blue curves denote the unconstrained, white-noise-constrained, and GM + constant solutions, respectively

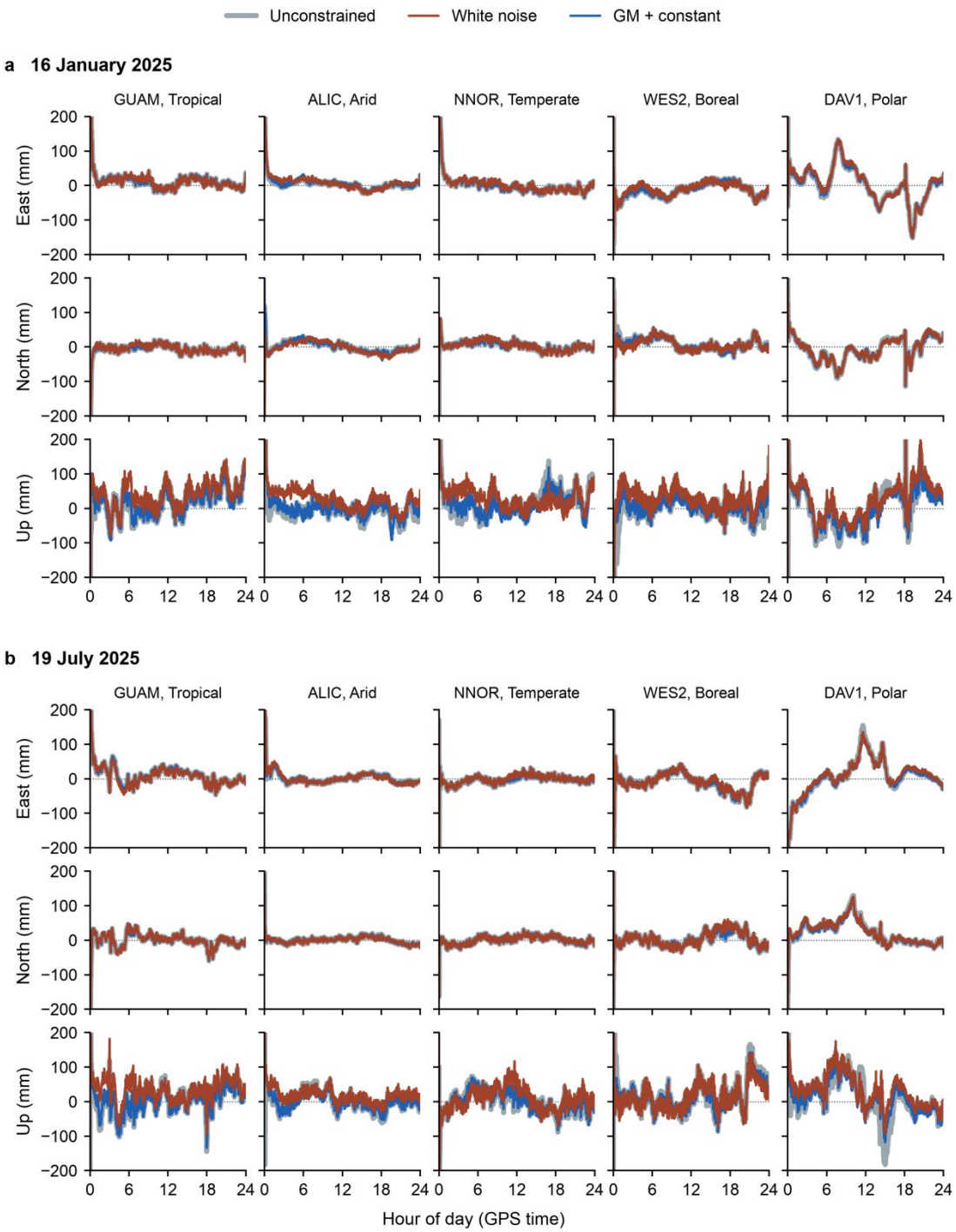


Fig. 5 East, north, and up coordinate errors for the kinematic PPP solutions at stations GUAM (tropical), ALIC (arid), NNOR (temperate), WES2 (boreal), and DAV1 (polar) on (a) 16 January 2025 and (b) 19 July 2025

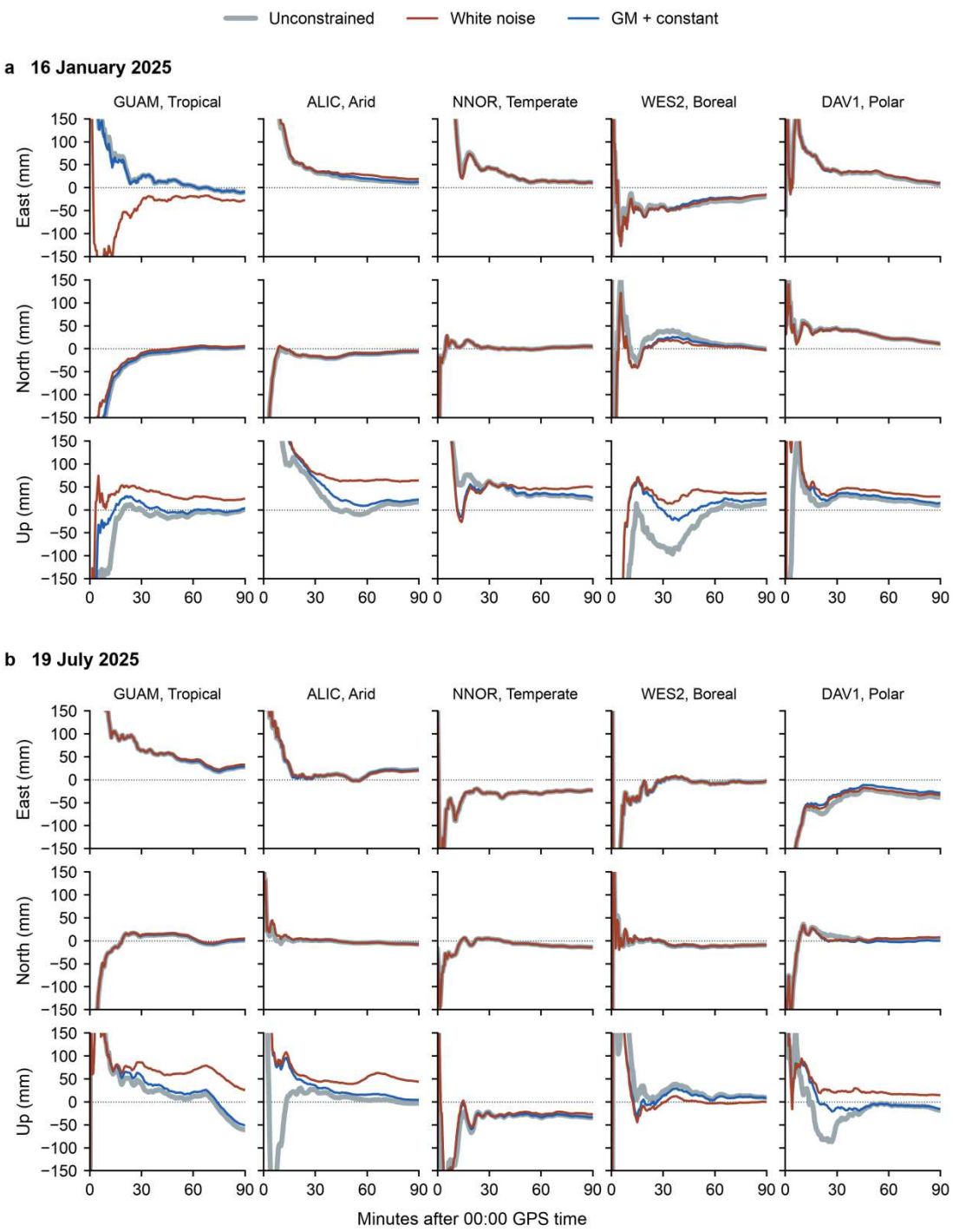


Fig. 6 Convergence-phase time series of east, north, and up coordinate errors for static PPP solutions at stations GUAM (tropical), ALIC (arid), NNOR (temperate), WES2 (boreal), and DAV1 (polar) on (a) 16 January 2025 and (b) 19 July 2025

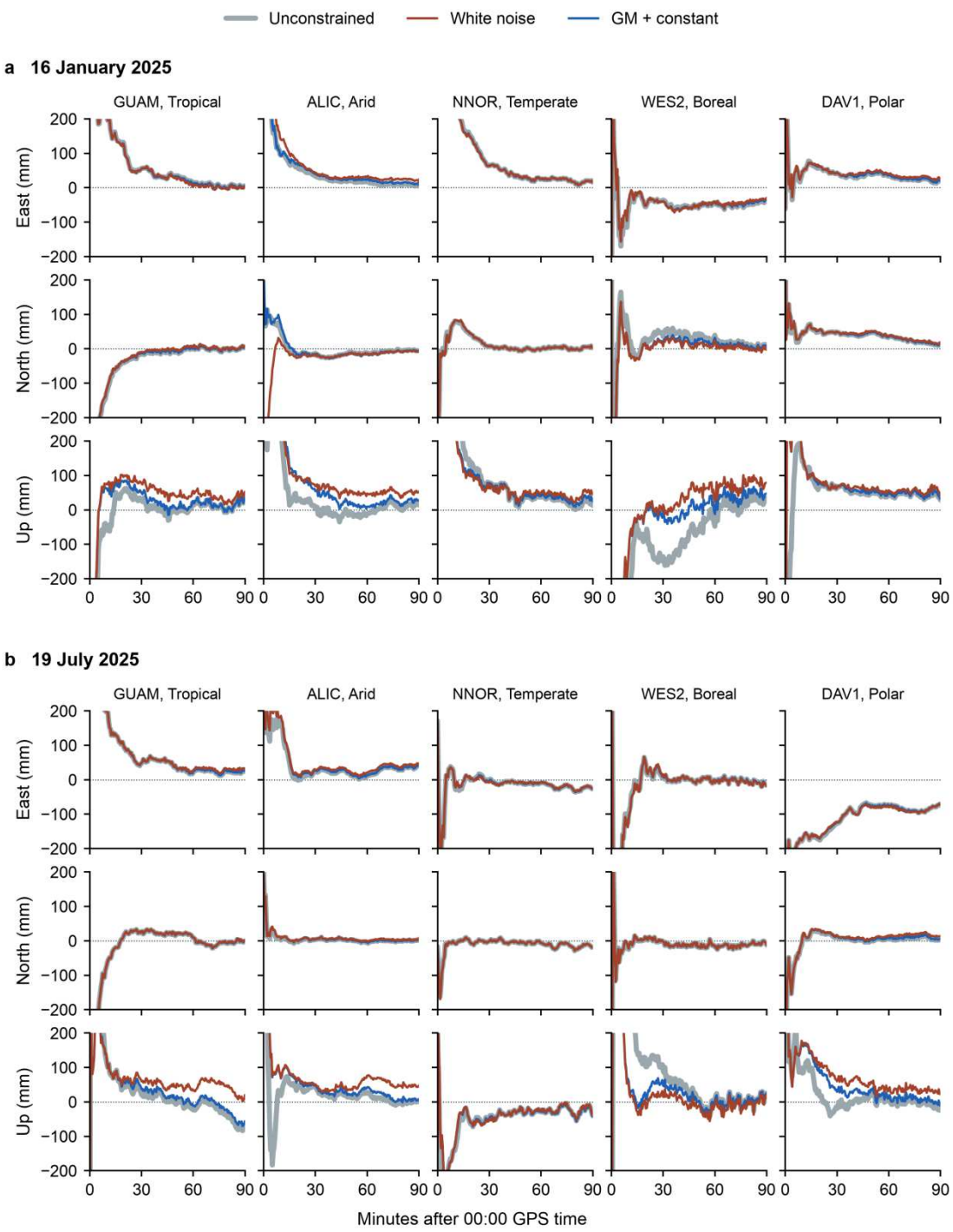


Fig. 7 Convergence-phase time series of east, north, and up coordinate errors for kinematic PPP solutions at stations GUAM (tropical), ALIC (arid), NNOR (temperate), WES2 (boreal), and DAV1 (polar) on (a) 16 January 2025 and (b) 19 July 2025

3.3 Information over-injection and ZTD-to-height error propagation

This section compares the suppression of ZTD-to-height error propagation under different constraint schemes. **Fig. 8** uses the full January and July 2025 dataset, with valid station-day

counts varying by scheme and processing mode (**Table 3**). The regression slope measures the sensitivity of the constraint-induced height shift to the arc-mean external ZTD error, not SINEX-referenced positioning accuracy. Under white-noise weighting, the measured slopes were −1.74 in static PPP and −1.93 in kinematic PPP. The predicted slope was within the 95% confidence interval in static mode but 0.02 outside it in kinematic mode.

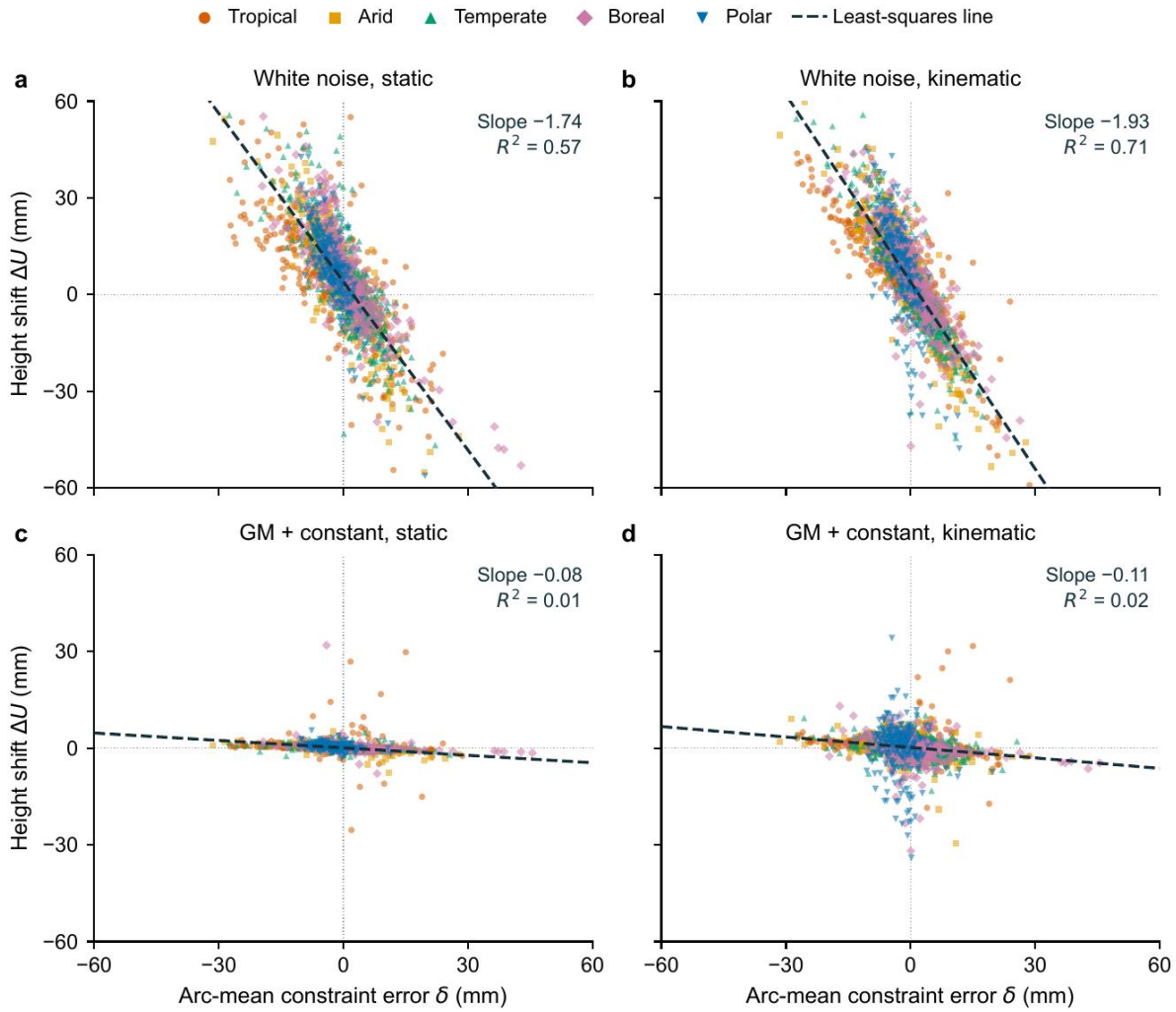


Fig. 8 Constraint-induced height shift ΔU relative to the corresponding unconstrained PPP solution against the arc-mean external ZTD error δ (diurnally corrected ERA5 ZTD minus IGS final ZTD, averaged over each daily arc) for station-days from January and July 2025, colored by climate band: **a** white noise, static; **b** white noise, kinematic; **c** GM + constant, static; **d** GM + constant, kinematic. Dashed lines are least-squares fits. Slope and R^2 are given in each panel

We next varied the constraint weight to test the predicted relationship between information share and height response. The variance-inflation scheme was evaluated in static mode using a matched 20-day subset of the full two-month dataset (10 days in January and 10 days in July 2025 across the 30 stations, yielding 580 common station-days for all settings) (Table 4). As the variance-inflation factor F increased from 1 to 1000, the external constraint's share of the ZTD information (γ) decreased from 50.5% to 0.2%, while the measured regression slope of height shift approached zero, changing from −1.69 to −0.01. At F = 65, the value motivated by the effective-sample-size analysis in Eqs. (15)–(16), γ was 2.3%, and the predicted and measured slopes were both approximately −0.07. The close agreement between predicted and measured slopes across the tested inflation factors supports the $\kappa\gamma$ relation, linking a lower constraint information share to a weaker height response to external ZTD errors.

Table 3 Closed-loop test of the leakage relation $\Delta U \approx \kappa \cdot \gamma \cdot \delta$. κ is the geometric coupling coefficient from the normal equations, *γ the share of the constraint in the ZTD estimate, measured in the ZTD domain*, and the measured slope is the least-squares slope of the constraint-induced height shift relative to the corresponding unconstrained PPP solution on the arc-mean external ZTD error δ (Fig. 8) with its 95% confidence interval across the full two-month dataset (1,813–1,822 static and 1,789–1,811 kinematic station-days)

Configuration	κ	γ (%)	Predicted $\kappa \cdot \gamma$	Measured slope [95% CI]	Within CI
White noise, static	−3.18	50.4	−1.60	−1.74 [−2.03, −1.51]	Yes
White noise, kinematic	−3.07	56.0	−1.72	−1.93 [−2.16, −1.74]	No
GM + constant, static	−3.18	1.8	−0.06	−0.08 [−0.15, −0.04]	Yes
GM + constant, kinematic	−3.07	3.3	−0.10	−0.11 [−0.14, −0.06]	Yes

The GM + constant scheme retained the early convergence benefit illustrated in Figs. 6 and 7 while largely suppressing the height response to external ZTD errors. The measured height-shift regression slopes were −0.08 in static PPP and −0.11 in kinematic PPP, with reductions of more than 94% in slope magnitude (Table 3) relative to the white-noise constraint solutions. The constraint's ZTD information shares were 1.8% and 3.3%, respectively, giving predicted slopes of −0.06 and −0.10 that agreed closely with the observations. The low R^2 values of 0.01 and 0.02 further indicate that only a weak linear association remained between arc-mean external ZTD errors and station-day height shifts. Using the corresponding unconstrained solution as the reference, the median absolute height shift $|\Delta U|$ over 2–24 h across the full two-month dataset decreased from 9.4 to 0.4 mm in static PPP and from 10.5 to 1.6 mm in kinematic PPP when white-noise weighting was replaced by GM + constant. The corresponding median absolute ZTD shift $|\Delta Z|$, also relative to the unconstrained solution, decreased from 2.64 to 0.25 mm in static PPP and from 2.97 to 0.48 mm in kinematic PPP.

Table 4 Information share and height-leakage slope across the variance-inflation ladder (static mode). All configurations (including F = 1 and GM + constant) are evaluated on the same 580 station-days from the 20-day variance-inflation subset (10 days per month), which accounts for the slight numerical differences relative to the full two-month dataset in **Table 3**. Predicted slopes are calculated using $\kappa = -3.1745$ and unrounded γ values. Differences are absolute differences calculated before rounding.

Inflation factor F	γ (%)	Predicted slope	Measured slope	Difference
1 (white noise)	50.5	−1.60	−1.69	0.09
4	23.6	−0.75	−0.78	0.03
16	8.1	−0.26	−0.26	0.00
65 (≈ N/Neff)	2.3	−0.07	−0.07	0.00
162 (Yao et al. 2017)	0.9	−0.03	−0.03	0.00
1000	0.2	−0.01	−0.01	0.00
GM + constant	2.0	−0.07	−0.05	0.02

We then compared the early positioning gains retained at similar levels of late-stage height-shift suppression. Of the 580 common static station-days, 568 passed the time-window coverage filter and were used for Fig. 9. On this matched subset, suppressing the 2–24 h median height shift ($|\Delta U|$) from 8.97 mm (F = 1) to the sub-millimeter level of GM + constant (0.34 mm) required F = 65–162 (0.39–0.16 mm; Fig. 9a). RMS height errors were computed relative to IGS SINEX coordinates, and reductions were calculated as the unconstrained RMS minus the constrained RMS. At these inflation factors, early-stage RMS reductions remained positive but were consistently smaller than those of GM + constant (Fig. 9b): over 0–15, 15–30, and 30–60 min, median reductions were 24.06, 8.53, and 2.55 mm for GM + constant versus 14.50, 2.91, and 0.73 mm for F = 65 (9.59, 1.27, and 0.34 mm for F = 162), with paired RMS differences

(RMS$_F$ − RMS$_{GM}$) of 5.29, 4.65, and 1.65 mm for F = 65 (all 95% CIs > 0).

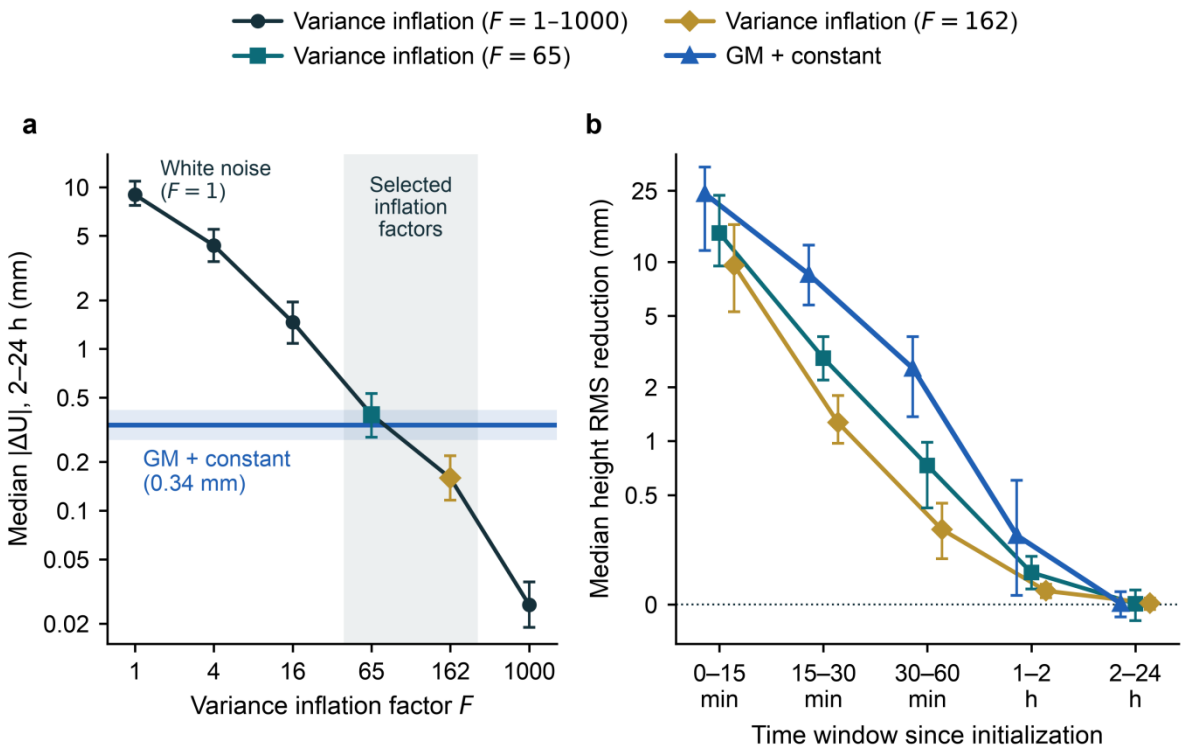


Fig. 9 Late-stage height shift and early-stage positioning gain in static PPP on 568 common station-days: **a** median absolute height shift (|ΔU|, 2–24 h) relative to unconstrained PPP versus inflation factor *F* (logarithmic axis); **b** median reduction in SINEX-referenced RMS height error relative to unconstrained PPP across time windows (symmetric logarithmic axis; lines are visual guides; error bars: 95% CIs)

3.4 Formal height uncertainty and positioning error

We next compare the filter-reported formal height uncertainties with SINEX-referenced empirical positioning errors to assess the discrepancy between nominal and empirical uncertainty metrics under different stochastic constraint models. In static PPP mode, the white-noise scheme yielded overly optimistic formal height standard deviations despite substantially larger SINEX-referenced height errors, as shown in Fig. 10. By the end of the daily arc, its median absolute height error remained around 13 mm, whereas the filter-reported formal standard deviation was only 2–3 mm because correlated constraints were repeatedly counted as

independent information. GM + constant reduced the median absolute height error to 6–7 mm, with a formal standard deviation of about 3 mm, substantially narrowing the gap between the nominal and empirical error metrics. Both quantities were close to those of the unconstrained solution. In kinematic PPP mode, GM + constant yielded height errors close to those of the unconstrained solution and lower than those under white-noise weighting, while formal standard deviations differed little among the three schemes.

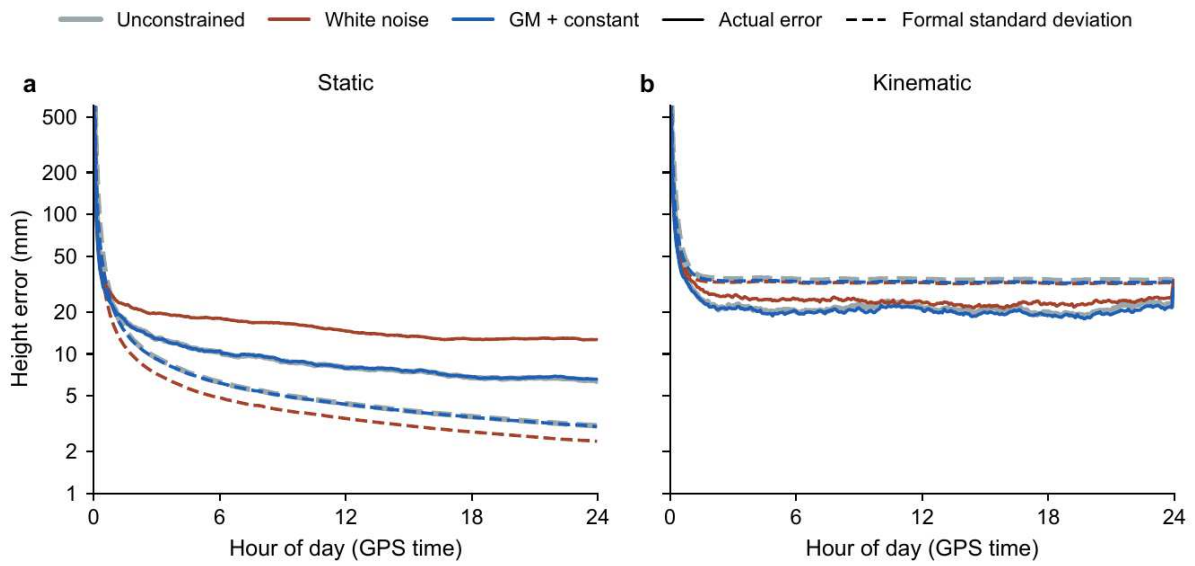


Fig. 10 Median absolute height errors relative to the IGS daily SINEX reference coordinates (solid lines) and formal height standard deviations (dashed lines) for the unconstrained, white-noise, and GM + constant schemes: a static PPP; b kinematic PPP. The vertical axis is logarithmic

3.5 Parameter sensitivity and network-wide parameterization

As illustrated in Fig. 11, the median absolute height error of the GM + constant scheme was relatively insensitive to the correlation time τ. Scaling τ from 0.25 to 4 times its identified value produced only small changes in this metric across the five climate bands. Reductions in RMS height error relative to unconstrained PPP over the 0.5–2 h window were retained in all climate bands except the polar band throughout the tested range, although their magnitude varied with

τ. Positive RMS reductions indicate improvement relative to the unconstrained PPP solution, whereas negative values indicate degradation.

In contrast, increasing σ_b reduced the median absolute height error across all five climate bands, while reductions in RMS height error over the 0.5–2 h window generally became smaller. At four times the identified value of σ_b, the RMS reductions relative to unconstrained PPP were small in all bands. These results indicate a trade-off between further reducing the median absolute height error and preserving the early positioning benefit of the external constraints

Replacing station-month-specific parameters with network-wide uniform values of τ, σ_b (155.1 min and 8.24 mm), or both yielded broadly comparable performance. Median absolute height errors remained low, and reductions in RMS height error over the 0.5–2 h window were generally maintained. Using a uniform σ_b increased the RMS reduction in the tropical band, whereas the benefit in the polar band remained limited. These findings support the use of common parameter values to simplify the configuration of the GM + constant scheme within the tested network.

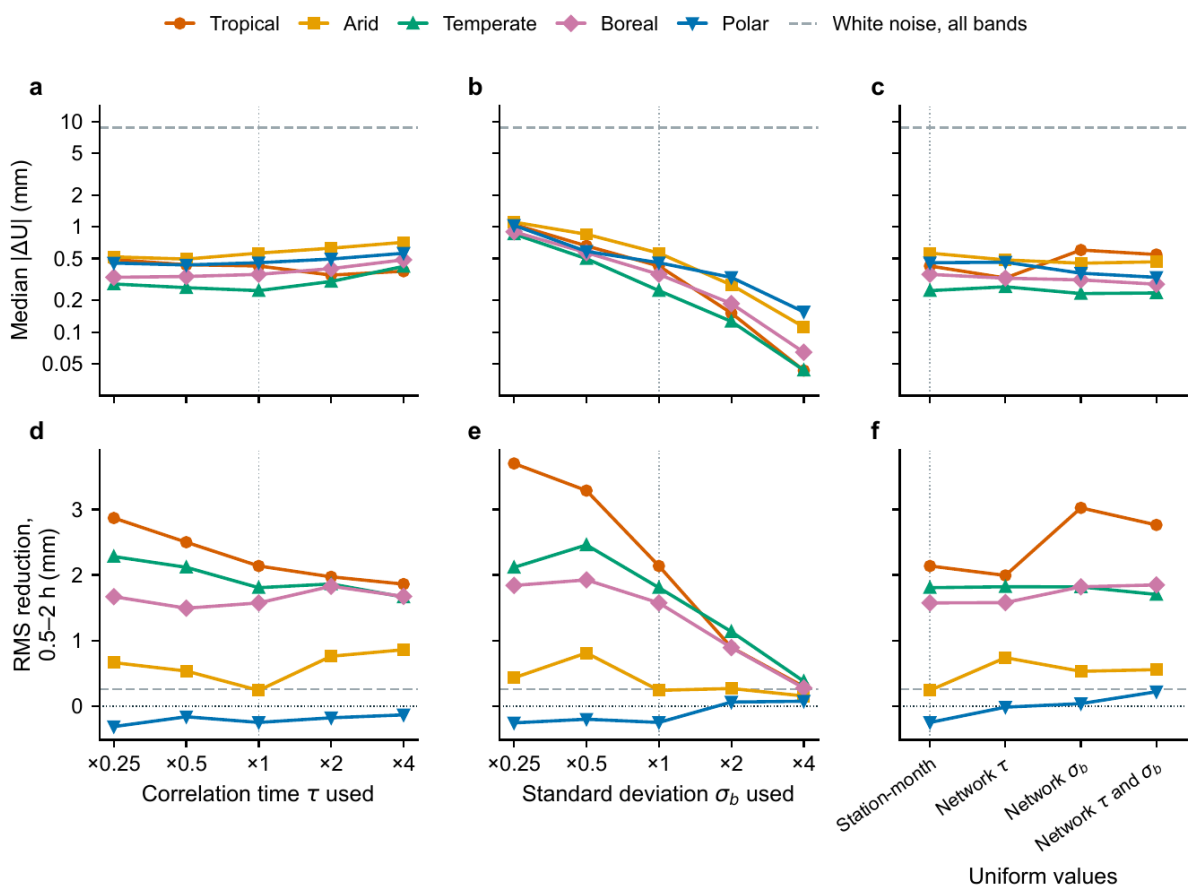


Fig. 11 Sensitivity of the GM + constant scheme to its parameters across climate bands. Top row: median absolute error in the PPP Up coordinate (|ΔU|) relative to the corresponding unconstrained PPP solution; bottom row: reduction in the root-mean-square (RMS) height error over the 0.5–2 h window relative to the unconstrained solution. **a, d** correlation time τ scaled from 0.25 to 4 times its identified value; **b, e** standard deviation σ_b scaled over the same range; **c, f** station-month-specific parameters replaced with network-wide uniform values. The dashed grey line represents the white-noise scheme for all climate bands. Vertical dotted lines indicate the identified parameter values

4 Discussion

The temporal correlation of external ZTD errors violates the epoch-wise independence assumption of the conventional white-noise formulation. When this correlation is neglected, redundant information in successive constraints is treated as independent evidence, leading to

information over-injection. Within individual daily arcs, the resulting excessive influence of non-zero arc-mean constraint error realizations on the ZTD estimate propagates to station height through the ZTD–height coupling, inducing persistent arc-level height shifts; across an ensemble of station-days, this stochastic model misspecification manifests as an inflated true error variance of the height estimator. This interpretation is supported by the general agreement between predicted and observed height-response slopes and by their attenuation as the constraint information share decreases. It also provides a statistical rationale for the empirical variance-inflation approach (Yao et al. 2017), which mitigates information over-injection associated with neglected temporal correlation.

However, variance inflation weakens the external ZTD constraints at all epochs and therefore reduces the retained early-stage convergence gain (Fig. 9). By contrast, the GM + constant model explicitly represents the temporal structure of the constraint errors, preserving a larger initial positioning benefit while similarly suppressing the height offsets. Motivated by the observed residual characteristics, the constant state accommodates persistent arc-level offsets, whereas the GM state captures correlated within-day fluctuations. These additional states represent errors in the external constraints rather than changes to the underlying ZTD dynamics. Accounting for this temporal dependence limits the repeated weighting of correlated errors as independent evidence while retaining the useful contribution of the external constraints. This approach is consistent with efforts to incorporate correction uncertainty and temporal correlation into PPP-RTK user filters (Khodabandeh et al. 2022), with the present analysis quantifying the link between external ZTD error structure and its impact on station height.

The practical benefits of this representation vary across stations and climate bands. This variability may reflect differences in both the constraint-error characteristics and the information already provided by GNSS observations, suggesting that the magnitude of the correlated error alone is insufficient to predict the resulting positioning gains. The sensitivity

analysis indicates that median absolute height errors are relatively insensitive to the correlation time, whereas the GM standard deviation governs the trade-off between height-error mitigation and early-stage positioning gains. The broadly comparable performance of network-wide and station–month-specific parameterizations further suggest that practical implementation may not require detailed parameter identification at each station: using fixed network-wide medians (τ = 155.1 min and σ_b = 8.24 mm) preserves nearly the full height-shift mitigation and early convergence gain without relying on in-sample station–month tuning. Independent validation across additional periods and external tropospheric products remains necessary to assess the transferability of this simplified parameterization and its suitability for real-time applications.

5 Conclusions

Neglecting temporal correlation in external ZTD errors leads to information over-injection, inducing arc-level PPP height shifts and inflating the true estimation error variance across arcs. For daily arcs with 300-s constraint updates, the effective-sample-size analysis indicated that the independence assumption overestimated the effective constraint information by approximately a factor of 65. A quantitative relation was derived linking external ZTD errors to height offsets through the constraint information share and ZTD–height coupling. Its explanatory value was supported by the general agreement between predicted and observed height-response slopes and their attenuation under variance inflation.

The proposed GM + constant model substantially reduced constraint-induced height offsets while retaining the early convergence benefit of external ZTD constraints. Relative to traditional white-noise ZTD constrained PPP, the magnitudes of the height-error regression slopes decreased from 1.74 to 0.08 in static PPP and from 1.93 to 0.11 in kinematic PPP, corresponding to reductions of more than 94% in both modes. These findings demonstrate that explicitly modeling the temporal structure of constraint errors can mitigate their impact on station height while preserving the useful contribution of external tropospheric constraints.

Statements and Declarations

Funding

This work was supported by Hong Kong Research Grants Council (RGC) General Research Fund (GRF) under Grant PolyU15212622/B-Q94L.

Competing interests

Zhizhao Liu is a member of the Editorial Advisory Board of GPS Solutions. The authors have no other relevant financial or non-financial interests to disclose.

Author contributions

Jing Wu: conceptualization, methodology, software, analysis, and writing—original draft.
Zhizhao Liu: supervision, resources, and writing—review and editing.

Data availability

The data presented in this study are available upon request from the corresponding author.

References

Aggrey J, Bisnath S (2019) Improving GNSS PPP convergence: the case of atmospheric-constrained, multi-GNSS PPP-AR. Sensors 19(3):587. https://doi.org/10.3390/s19030587

Bayley GV, Hammersley JM (1946) The "Effective" Number of Independent Observations in an Autocorrelated Time Series. Journal of the Royal Statistical Society Series B: Statistical Methodology 8(2):184–197. https://doi.org/10.2307/2983560

Bock O, Parracho AC (2019) Consistency and representativeness of integrated water vapour from ground-based GPS observations and ERA-Interim reanalysis. Atmos Chem Phys 19(14):9453–9468. https://doi.org/10.5194/acp-19-9453-2019

Dehvari M, Farzaneh S, Forootan E (2025) Optimizing PPP Performance by Incorporating ZWD Constraints Derived From Data Assimilation. Earth and Space Science 12(8):e2024EA004173. https://doi.org/10.1029/2024EA004173

621 Deng Y, Chen W, Ding J, El-Mowafy A, Weng D, Tang L, Bai L, Mi X (2026) Improving
622 GNSS precise point positioning with tropospheric constraints from data-driven numerical
623 weather prediction model. Geo-spatial Information Science 29(1):678–695.
624 https://doi.org/10.1080/10095020.2025.2513650
625 Gallon E, Joerger M, Pervan B (2021) Robust Modeling of GNSS Tropospheric Delay
626 Dynamics. IEEE Trans Aerosp Electron Syst 57(5):2992–3003.
627 https://doi.org/10.1109/TAES.2021.3068441
628 Gao R, Liu Z, Odolinski R, Zhang B (2024) Improving GNSS PPP-RTK through global
629 forecast system zenith wet delay augmentation. GPS Solut 28(2):66.
630 https://doi.org/10.1007/s10291-023-01608-0
631 Huang L, Liu F, Guo L, Lan G, Zhou L, Wang C, Liu L (2023) An ERA5 tropospheric
632 parameters-augmented approach for improving GNSS precise point positioning. Geodesy and
633 Geodynamics 14(5):467–476. https://doi.org/10.1016/j.geog.2023.01.004
634 Ibrahim HE, El-Rabbany A (2011) Performance analysis of NOAA tropospheric signal delay
635 model. Meas Sci Technol 22(11):115107. https://doi.org/10.1088/0957-0233/22/11/115107
636 Kalman RE (1960) A New Approach to Linear Filtering and Prediction Problems. Journal of
637 Basic Engineering 82(1):35–45. https://doi.org/10.1115/1.3662552
638 Khodabandeh A, Teunissen PJG, Psychas D (2022) On the Problem of Double-Filtering in
639 PPP-RTK. Sensors 23(1):229. https://doi.org/10.3390/s23010229
640 Kouba J, Héroux P (2001) Precise Point Positioning Using IGS Orbit and Clock Products.
641 GPS Solut 5(2):12–28. https://doi.org/10.1007/PL00012883
642 Li X, Zus F, Lu C, Dick G, Ning T, Ge M, Wickert J, Schuh H (2015) Retrieving of
643 atmospheric parameters from multi-GNSS in real time: Validation with water vapor
644 radiometer and numerical weather model. Journal of Geophysical Research: Atmospheres
645 120(14):7189–7204. https://doi.org/10.1002/2015JD023454

646 Lu C, Zus F, Ge M, Heinkelmann R, Dick G, Wickert J, Schuh H (2016) Tropospheric delay
647 parameters from numerical weather models for multi-GNSS precise positioning. Atmos Meas
648 Tech 9(12):5965–5973. https://doi.org/10.5194/amt-9-5965-2016
649 Ma X, Wang X, Yao Y, Zhu H, Zhang B, Chu R, Zhang Q, Feng Y (2025) Enhanced multi-
650 GNSS precise point positioning based on ERA5 precipitation water vapor information. J Geod
651 99(3):24. https://doi.org/10.1007/s00190-025-01948-4
652 Niell AE (1996) Global mapping functions for the atmosphere delay at radio wavelengths. J
653 Geophys Res 101(B2):3227–3246. https://doi.org/10.1029/95JB03048
654 Saastamoinen J (1972) Atmospheric Correction for the Troposphere and Stratosphere in
655 Radio Ranging Satellites. In: Henriksen SW, Mancini A, Chovitz BH (eds) Geophysical
656 Monograph Series. American Geophysical Union, Washington, D. C., pp 247–251
657 Santerre R (1991) Impact of GPS satellite sky distribution. Manuscr Geod 16(1):28–53.
658 https://doi.org/10.1007/BF03655285
659 Shi J, Xu C, Guo J, Gao Y (2014) Local troposphere augmentation for real-time precise point
660 positioning. Earth Planet Sp 66(1):30. https://doi.org/10.1186/1880-5981-66-30
661 Simon D (2006) Optimal state estimation: Kalman, H∞, and nonlinear approaches. John
662 Wiley & Sons, Hoboken. https://doi.org/10.1002/0470045345
663 Tralli DM, Lichten SM (1990) Stochastic estimation of tropospheric path delays in global
664 positioning system geodetic measurements. Bull Geodesique 64(2):127–159.
665 https://doi.org/10.1007/BF02520642
666 Wilgan K, Hadas T, Hordyniec P, Bosy J (2017) Real-time precise point positioning
667 augmented with high-resolution numerical weather prediction model. GPS Solut 21(3):1341–
668 1353. https://doi.org/10.1007/s10291-017-0617-6
669 Yao Y, Peng W, Xu C, Cheng S (2017) Enhancing real-time precise point positioning with
670 zenith troposphere delay products and the determination of corresponding tropospheric

671 stochastic models. Geophys J Int 208(2):1217–1230. https://doi.org/10.1093/gji/ggw451

672
673

Author biographies

Jing Wu is a PhD candidate in the Department of Land Surveying and Geospatial Science at The Hong Kong Polytechnic University. He received his M.Sc. from the Chinese Academy of Sciences. His research focuses on tropospheric modeling and global navigation satellite system precise point positioning, including the effects of external tropospheric constraints.

Zhizhao Liu is a Professor in the Department of Land Surveying and Geospatial Science at The Hong Kong Polytechnic University. He received his PhD in Geomatics Engineering from the University of Calgary in 2004. His research interests include global navigation satellite systems, atmospheric remote sensing, meteorology, and high-precision satellite positioning.

Supplementary Files

This is a list of supplementary files associated with this preprint. Click to download.

- GPSSsupplementaryinfo1.pdf